The Λ-invariant and topological pathways to influence the strength of sub-micron crystals

Stefanos Papanikolaou[1,2,*] and Giacomo Po[3]

[1] *Department of Mechanical & Aerospace Engineering, West Virginia University, 395 Evansdale Drive, Morgantown, WV, 26506-6070.*
[2] *Department of Physics & Astronomy, West Virginia University, 135 Willey St, Morgantown, WV 26506-6070.*
[3] *Department of Mechanical & Aerospace Engineering, University of Miami, 1251 Memorial Drive, Coral Gables, FL 33146*

(Dated: April 16, 2020)

In small volumes, sample dimensions are known to strongly influence mechanical behavior, especially strength and crystal plasticity. This correlation fades away at the so-called *mesoscale*, loosely defined at several micrometers in both experiments and simulations. However, this picture depends on the *entanglement* of the initial defect configuration. In this paper, we study the effect of dislocation topology, through the use of a novel observable for dislocation ensembles, the Λ-invariant, that depends only on mutual dislocation linking: It is built on the natural vortex character of dislocations and it has a continuum/discrete correspondence that may assist multiscale modeling descriptions. We investigate arbitrarily complex initial dislocation microstructures in sub-micron-sized pillars, using three-dimensional discrete dislocation dynamics simulations for finite volumes. We demonstrate how to engineer nanoscale dislocation ensembles that are independent from sample dimensions, either by biased-random dislocation loop deposition or by sequential mechanical loads of compression and torsion.

Among the most remarkable aspects of forming processes in metals is the ability to manipulate material strength by "cold working" [1]. At the heart of this versatile feature lies the ability of crystal defects, especially dislocations [2, 3], to interact collectively, develop entangled microstructures and multiply. Dislocation entanglement has been notoriously believed to control a plethora of phenomena in metallurgy, including forest and kinematic hardening, as well as fatigue [4]. However, the paramount importance of dislocation entanglement only became clear in the study of small finite volumes, by noticing the dramatic effects of its absence [5–11]: Crystalline strength drastically increases when at least one dimension decreases below the so-called *mesoscale*, which loosely refers to a few micrometers [12–16] where dislocations may define their "mean-free path" [13]. Nevertheless, crystal dislocations typically form loops that may easily extend to the volume boundaries, and thus mutual dislocation topologies may be critical. In addition, mechanical yielding is a transient behavior that ought to strongly depend on initial conditions, especially in small volumes [17]. In this work, we show that dislocation entanglement originates in dislocation loops' topology and not particular length scales. We investigate the possible effects of initial conditions by constructing a topological observable of dislocation networks, the Λ-invariant, that is only dependent on mutual loop entanglement. We show that the Λ-invariant can be used to generate arbitrarily complex microstructures in Discrete Dislocation Dynamics (DDD) simulations [18–23], either by deposition or cold-working, rendering a sub-micron volume capable of yielding akin to a bulk sample. In this way, we may identify topological pathways to manage strength and crystal plasticity.

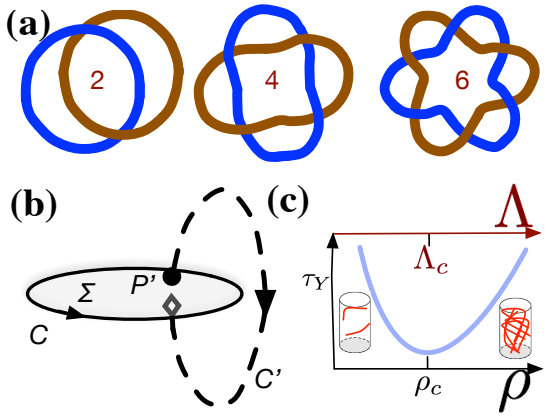

FIG. 1. **Dislocation Loops and Topology**. (a) Two dislocation loops on different slip systems can form a topological *link* with linking number 2, 4 or 6 depending on the activation of additional latent hardening mechanisms such as double cross-slip. (b) The *linking number* can be directly calculated through a dislocation line double integral, the Gauss integral (see text). (c) The shear strength τ_Y of a submicron finite volume is typically viewed in the $\tau_Y - \rho$ space [24] introducing the elusive concept of the dislocation "mesoscale", defined at a critical ρ_c. Hereby, we propose that a topological measure might provide a clear understanding of why a transition takes place, from low to high dislocation densities.

Crystal plasticity modeling represents an enormous challenge of materials science despite the understanding of basic interactions and mechanisms of individual dislocations. For example, the "back-stress" in theories of kinematic and work hardening [1] does not yet

have a precise microscopic definition [25, 26]. In fact, the great complexity of crystal plasticity theories originates in that dislocation ensembles are more akin to a "bird's nest", rather than a set of separate small and simpler elementary bodies [27]. In sub-micron-sized volumes, where it becomes tough to fit such a nest, common plasticity practically disappears, giving its place to uncommon size effects and stochasticity in the mechanical response [9, 28, 29]. In association, prior deformation of a micropillar before testing [30] may turn size effects into Taylor hardening (*cf.* Fig. 1(c)), as dislocation density increases [24]. However, another plausible interpretation is that dislocation *complexity* is the key, in a small finite volume, that may unlock common plasticity. In such a scenario, the inflection point Λ_c has a fundamental importance in terms of topological complexity, possibly revealing how many dislocation "twigs" need to intertwine to start behaving as a bird's nest.

We present a novel approach to characterize and engineer dislocation entanglement that naturally translates into continuum and large-deformation descriptions of dislocation ensembles. Our basis is the construction of a scalar volume observable, dubbed Λ-invariant, which has special topological properties, thus leaping beyond the distortion (elastic/plastic) or dislocation density tensors [2]. The purpose of Λ is to sum the linking number of each pair of dislocation loops in the ensemble.

The *Linking Number* for two dislocation loops i and j is defined as $L_{ij} = \frac{1}{4\pi}\int_{C_i}\int_{C_j} d\Omega(\mathbf{r}_i,\mathbf{r}_j) \equiv \frac{1}{4\pi}\int_{C_i}\int_{C_j}\frac{(d\mathbf{r}_j\times d\mathbf{r}_i)\mathbf{r}_{ij}}{r_{ij}^3}$ [31, 32], where $\int_{C_i}$ implies an integral over the loop i. It is a plausible way to define the mutual entanglement of a pair of dislocation loops (*cf.* Fig. 1(b)): A linking number of 2 is typical for crossing dislocations in different slip systems, while higher linking numbers require additional consecutive mechanisms such as consercutive double cross-slip events (*cf.* Fig. 1(a)). The topological character of the linking number originates in that it does not depend on local line distortions, thus it does not explicitly relate to dislocation *length* density. In this way, it complements common dislocation network observables. Numerically, L_{ij} can be calculated directly through counting solid angle contributions around the two loops i, j [33].

The Λ-invariant in a crystal of Burgers vector magnitude b is defined as,

$$\Lambda = \frac{1}{b^2}\int d^3x\beta^E\cdot(\nabla\times\beta^E) = \frac{1}{b^2}\int d^3x\beta^E_{ij}\alpha_{ij} \quad (1)$$

where α is the Nye dislocation density tensor and the elastic distortion β^E combines with the plastic distortion β^P to give $\beta^P+\beta^E = grad(u)$, where u is the displacement field due to deformation [1, 2], ultimately satisfying on a closed crystal boundary Γ

$$\alpha = \nabla\times\beta^E = -\nabla\times\beta^P = \delta_\Gamma\otimes\vec{b} \quad (2)$$

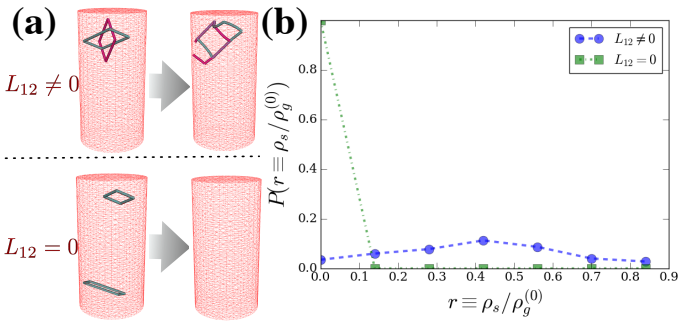

FIG. 2. **Statistics of two loops in a 0.5μm-pillar**: (a) Initial conditions of i) two prismatic dislocation loops 1 and 2, with randomly selected Burgers vectors but finite L_{12}, ii) two prismatic dislocation loops 1 and 2, with randomly selected Burgers vectors but zero L_{12}. (b) Probability of forming sessile dislocation junctions through 2 randomly placed prismatic loops with or without linking.

This defining vortex character of dislocations signifies that dislocations maintain a *loop* character that may not end within the crystal. By using this feature, one may show (see Supplementary Information (SI) [34, 35] that

$$\Lambda = -\frac{1}{b^2}\sum_{i,j}L_{ij}\mathbf{b}_i\cdot\mathbf{b}_j \quad (3)$$

where L_{ij} is the linking number between loops i and j, while $\mathbf{b}_i$ and $\mathbf{b}_j$ are their respective Burgers vectors. The mathematical structure of Λ resembles that of helicity in theories of fluids. However, Λ is never a conserved integral of the equations of motion in a limiting scenario, in contrast to helicity.[34–36]

The primary usefulness of Λ is its capacity of predicting the onset of dislocation multiplication through dislocation junction formation. The connection between finite Λ and junction formation can be seen in two ways: First, the absence of linking ($L_{ij}=0$) leads to a negligible *statistical* probability for junction formation, especially in small finite volumes. Second, the dependence of Λ on the linking loops' Burgers vectors' dot product point directly to a junction-formation energetic connection to the Frank rule. A way to realize different possibilities is to consider prismatic dislocation loops, which have been connected to hardening effects in various circumstances [37, 38]. We consider two prismatic dislocation loops randomly placed in a $D=0.5\mu$m-diameter pillar (see Fig. 2(a)), and we generate 10^4 random initializations of two dipolar prismatic loops, constrained to either have mutual linking number L_{12} zero or nonzero, signifying initial dislocation entanglement or not. Then, the configuration is relaxed by using DDD. Then, the histogram of *sessile* dislocation junction formation (see Fig. 2(b)) displays significant junction length formation only for finite entanglement ($L_{12}\neq 0$), with a wide probability distribution that remarkably overwhelms the

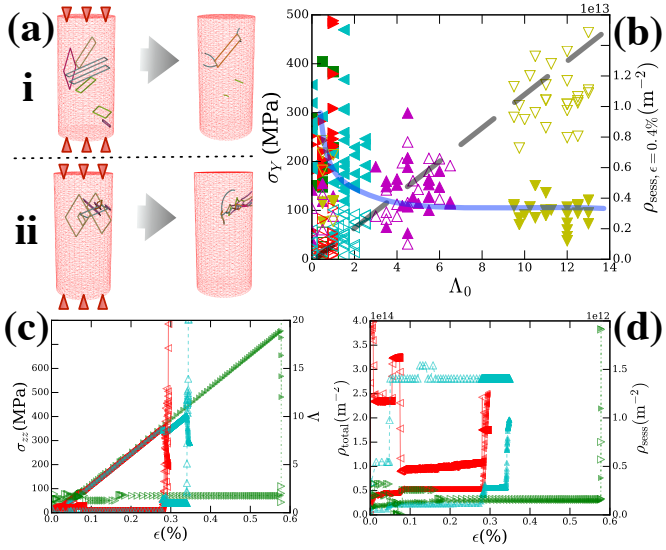

FIG. 3. **Depositing & Testing Entanglement For Various Discrete Dislocation Densities: Uniaxial compression of sub-micron volumes.** Initial sessile junction density is always zero. **(a)** Random deposition and uniaxial compression of prismatic dislocation loops in a finite mesh of $R = 0.25\mu$m in (i) an unbiased or (ii) Λ-biased manner. (shown compression to 0.01% strain for $\rho_0 = 2 \times 10^{13}/\text{m}^2$ (various ρ_0 choices are studied), **(b)** Nanopillar yield stress (solid symbols) and sessile dislocation density (open symbols) at 0.4% strain as function of initial Λ_0. Every point corresponds to a uniaxial compression simulation of distinct initial conditions at a target ρ_0: ($\rho_0 : \{\blacksquare : 10^{13}/\text{m}^2\}$, $\{\blacktriangleright : 2 \times 10^{13}/\text{m}^2\}$, $\{\blacktriangleleft : 4 \times 10^{13}/\text{m}^2\}$, $\{\blacktriangle : 8 \times 10^{13}/\text{m}^2\}$, $\{\blacktriangledown : 10^{14}/\text{m}^2\}$). In **(c)** and **(d)**, an excerpt of the response of three sample initial conditions are shown in detail to demonstrate the major effect that heavily entangled have on mechanical response. The loading stress σ_{zz} as function of the applied axial zz strain ϵ is shown in **(c)** with solid symbols. The Λ configurational value as function of the applied axial zz strain ϵ is shown in **(c)** with open symbols. Analogously, in **(d)**, the total (open) and sessile (closed) dislocation density are shown. The sessile dislocation density increases roughly linearly with Λ_0 while yield stress quickly saturates. ρ_0 values are given for the configurations used in **(c)** and **(d)**: ($\{\blacktriangle : 8 \times 10^{12}/\text{m}^2\}$, $\{\blacktriangleright : 10^{13}/\text{m}^2\}$, $\{\blacktriangleleft : 2 \times 10^{13}/\text{m}^2\}$).

disentangled ($L_{12} = 0$) configurations. Segment-based junction formation arguments [39, 40] (*ie.* nearby straight lines) may partially explain the statistics in Fig. 2(b), but the scenario of two intertwining dislocation loops is different in that all possible signs of dislocation interactions are present in a linked dislocation pair. Thus, it is natural to expect a significantly larger *statistical* preference towards sessile junction formation for linked loops than two nearby straight lines [41, 42]

The statistical finding for the fate of two linked loops has significant consequences for the behavior of collective dislocation networks. By using a numerical algorithm that explicitly tracks the evolution of dislocation loops and segments [18–23] and their mutual linking numbers, we are able to arbitrarily tune the complexity of the initially deposited dislocation configuration. When a junction forms, we assume that Λ remains unchanged, thus Λ's history is critical to its determination. We consider the geometry of a cylindrical nanopillar finite element mesh of diameters $D \times 10^{-3}/b = 2, 4, 8, 16, 32$ for single crystalline Cu FCC with $|\mathbf{b}| = 0.2556$nm. We generate random prismatic loop initial conditions by depositing prismatic dislocation loops of randomly selected Burgers vectors in the nanopillar until a target dislocation density ρ_0 is reached (see *e.g.* Fig. 3(a) for $\rho_0 = 10^{13}/\text{m}^2$). By biasing the deposition of prismatic loops towards collectively increasing Λ, we acquire control on the investigation of topological effects. ρ_0 is varied in the range of $10^{12} - 10^{14}(/\text{m}^2)$, and loading at a strain rate $10^3/s$ is along the cylindrical axis.

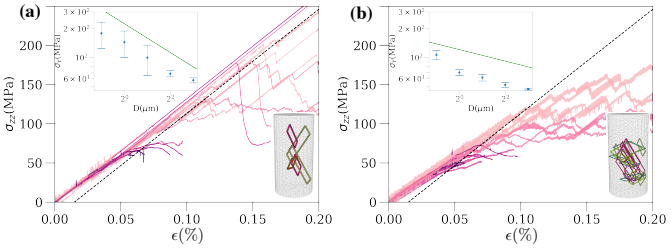

FIG. 4. **Uniaxial Compresion Size Effects and** Λ: 4 realizations at each size with initially random dislocation density constrained so that **(a)** $\Lambda < 2$ and **(b)** $\Lambda > 3$. Each color corresponds to a sample size with diameter $D = 0.5, 1, 2, 4, 8\mu$m. Color darkness increases with D. The insets show the engineering yield stress (defined at 0.02% plastic strain), with power law lines $\sim D^{-0.5}$(left) and $D^{-0.2}$(right). Also, an initial configuration is shown for $D = 1\mu$m for small and large Λ (see also SI).

The effect of topologically rich initial conditions is drastic in material properties such as the compressive yield strength (*cf.* Fig. 3(b)), defined as the first axial zz stress at which a large ($>$ 1MPa) stress drop avalanche event is observed. For large initial Λ_0 (in this work, we focus on Λ's magnitude), in fact, the strength of the pillars is dominated by the microstructure entanglement as opposed to the sample size, leading to a linear increase of the sessile dislocation density at an arbitrarily chosen 0.4% finite strain ($\rho_{sess} \sim \Lambda_0$). While this is only evidence of a scaling relation between Λ_0 and dislocation densities in small finite volumes, we expect that the scaling relationship $\rho_{sess}(\epsilon) \sim \Lambda_0^\delta$ for $\delta \geq 0$ generically holds for any dislocation ensemble. Plastic yielding in these systems is accompanied by large Λ-"avalanches" (*cf.* Fig. 3(c)), caused by large increase in the density of *sessile* junctions (*cf.* Fig. 3(d)), and subsequent multiplication to increase the total dislocation density (*cf.* Fig. 3(d)). Overall, this behavior should be contrasted to the typically observed mechanism-exhaustion-

dominated one in analogously small finite volumes [29], which in our simulations can be seen only for $\Lambda \lesssim 2$, found from an exponential fit to the data's variance in Figs. 3(b), 5(b). The effect of $\Lambda_c \simeq 2$ becomes evident when size effects are found for samples with initial configurations of $\Lambda_0 < 2$ (see Fig. 4(a) and its inset), resembling prior studies [5–11] with a size dependence of strength $\sigma_Y \sim D^{-0.5}$. Characteristically, when $\Lambda_0 < 2$ (*cf.* Fig. 4(a)), perfect elastic response is often observed after the initially placed dislocations deposit on the pillar surface. This behavior is contrasted to samples with initial $\Lambda_0 \gg 2$ (see Fig. 4(b) and its inset), showing virtual size independence ($\sigma_Y \sim D^{-0.2}$) and relatively consistent response (see also SI).

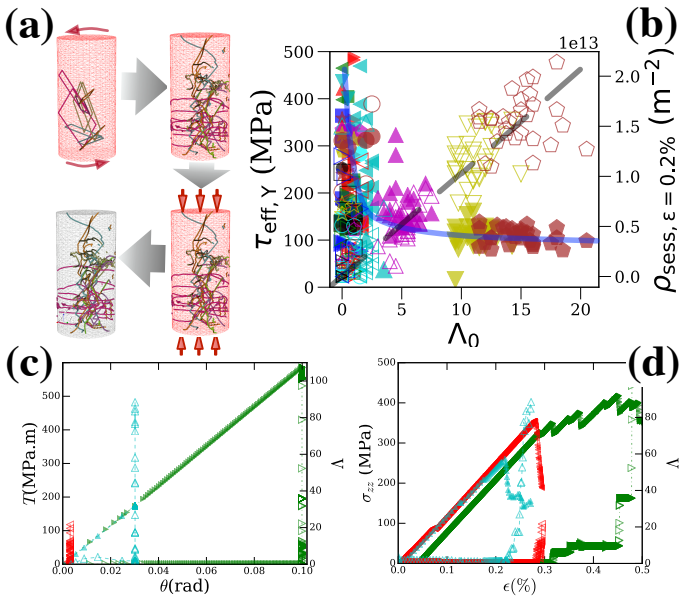

FIG. 5. **Engineering Entanglement By Controlling Prior Torsion Strains: Uniaxial compression of sub-micron volumes**. **(a)** A protocol is followed where a dislocation loop configuration at density ρ_0 is prepared, torsion is applied on top/bottom pillar surfaces up to pre-chosen torsion angle θ_0, and then uniaxial compression is applied towards yield. The configurations at each step of the process are shown for a particular configuration with $\rho_0 = 3 \times 10^{13}/\text{m}^2$. **(b)** Yield stress (left y-scale/filled symbols) and sessile dislocation density (right y-scale/open symbols) at the yield point *vs.* Λ_0 for a variety of initial conditions and torsions $\rho_0 \in (5 \times 10^{12}, 2 \times 10^{14})$ and $\theta_0 \in \{10^{-5}, 0.1\}$. In (c,d) three characteristic cases $\{\rho_0, \theta_0\} \rightarrow \Big(\blacktriangleright$: $[10^{13}/\text{m}^2, 0.1]$, $\blacktriangleleft$: $[2 \times 10^{13}/\text{m}^2, 3 \times 10^{-3}]$, $\blacktriangle$: $[2 \times 10^{13}/\text{m}^2, 3 \times 10^{-2}]\Big)$, are shown for **(c)** Torsion T (filled symbols) and Λ (open symbols) *vs.* torsion angle θ and **(d)** subsequent loading stress σ_{zz} (filled symbols) and Λ (open symbols) *vs.* axial strain ϵ.

Besides artificial deposition of initial dislocation configurations with dramatic effects on mechanical properties, the topological character of Λ may guide us towards generating large-entanglement structures through particularly *efficient* mechanical loading paths. These loading paths can be also predicted through modeling of latent hardening for particular crystalline structure [43]. The key towards identifying such loading paths is the calculation of the Λ-dynamics. For a large class of continuum dislocation theories that satisfy global Burgers vector conservation and Orowan's law of collective dislocation motion, it may be shown that (see SI),

$$\frac{\partial \Lambda}{\partial t} = \frac{1}{b^2} \int_{\partial V} dS_j \epsilon_{jkm} \beta^E_{kl} J_{ml} \tag{4}$$

where the typical assumption of overdamped dynamics is considered and $J_{ij} = \epsilon_{ikm} F_m \alpha_{kj}$, where F_m is the Peach-Koehler force on the dislocation density α_{kj}. The tensorial character of the right-hand side of Eq. 4 implies that only particular loading directions can increase Λ, a fact well known from studies of latent hardening in crystal plasticity [13, 44–46]. A physically intuitive example is the uniaxial compression of pre-torsioned specimens, where dislocation flow J_{ij} may be assumed in a pre-strained environment to a torsion angle θ_0, with induced β^E along the cylindrical θ direction (*ie.* $\partial_x u_z$ and $\partial_y u_z$ are non-zero) while $\mathbf{t} \times \mathbf{v}$ for an x-y gliding dislocation would be along $\mathbf{z}$ during compression. This combination of indices gives a concrete contribution to the right-hand-side integral of Eq. 4. Physically, in the idealized continuum cases, torsion induces geometrically imposed screw dislocations along the torsion axis. It is expected that torsion-induced screw dislocations along the loading axis would tangle with horizontal-moving slip during subsequent compression, and this is what Eq. 4 is predicting.

To confirm the approach towards the generation of Λ, we perform explicit 3D-DDD sequential-loading simulations of submicron-sized pillars with various initial dislocation densities ρ_0. We vary ρ_0 from $5 \times 10^{12}/\text{m}^2$ to $3 \times 10^{14}/\text{m}^2$. We consider an initial configuration of randomly deposited dipolar dislocation loops in a 2000b-diameter cylindrical pillar, and then we consider the application of a finite torsion angle on the top and bottom surfaces as a boundary condition that we progressively implement at a low torsion rate of 10^{-3}rad/s. Then, the torsion angle is fixed and, uniaxial pillar compression along the $z-$axis is considered. As shown in Fig. 5(a), the application of a finite amount of torsion (which may not be necessarily large enough to induce plasticity) on the top/bottom surfaces up to a target torsion angle θ_0 ($\in (0, 0.1)$), leads to a highly extended dislocation configuration that generates large entanglement when it is followed by uniaxial compression, as it is witnessed by the increase of Λ. Characteristically, if one calculates the combined-loading effective stress, then the yield stress is remarkably size-independent (*cf.* Fig. 5(b)) and the saturation level for the sessile dislocation density is easily reached, even with small initial Λ and initial dislocation density. As one may see in particular exam-

ples (*cf.* Fig. 5(c),(d)), the application of torsion is followed with a dramatic increase of Λ, as suspected by our developed topological intuition. Namely, prior applied torsion at a target θ_0 (three distinct realizations at $\theta_0 = 0.001, 0.01, 0.1$ are shown in Fig. 5(c)) leads to a large increase of Λ at values much larger (> 50) than the ones observed in the highly-entangled deposition of Fig. 3, and forming visible networks of system-spanning screw dislocations that necessarily would form junctions to any dominant-slip gliding dislocations during subsequent uniaxial zz compression.

The usefulness of Λ is not limited to the characterization and prediction of discrete and entangled dislocation networks, but also it extends to represent a unique *discrete-continuum* link that can be directly calculated in both the discrete and the continuum worlds. In the continuum, it is just needed to properly estimate a β^E-dependent volume integral. Its topological origin also allows us to write the correspondent of Λ for large deformations. Following Ref. [47] a large deformation generalization may be shown to be (see SI),

$$\Lambda = \frac{1}{b^2} \int J^e \mathbf{F^{e-1}} \cdot (\nabla \times \mathbf{F^{e-1}})^{-\tau} \cdot \mathbf{F^{e-\tau}} d\tilde{V} \qquad (5)$$

where $\mathbf{F^{e-1}}$ is defined by the Kröner-Lee decomposition [48, 49]: $\mathbf{F} = \mathbf{F^e F^p}$ and $J^e = \det \mathbf{F^e}$ (see SI). In this way, Λ may be instrumental for extending dislocations' role towards modeling of large deformations.

In conclusion, we presented a topological approach to investigate dislocation entanglement [50] and latent hardening in crystals. In this work, we investigated random initial conditions composed of dipolar prismatic loops. We find that the manipulation of initially prepared dislocation configurations' topological complexity can generate *size independent* crystal plasticity even in nanoscale volumes, that are believed to be *intrinsically* size-dependent [51, 52]. This manipulation and control of dislocation networks may allow for optimization and design of multi-axial, sequential cold-working pathways in metallurgy [53, 54], especially by unveiling the connections between junction formation rate, flow stress and Λ.

We would like to thank J. Bassani, N. Ghoniem and E. Van der Giessen for inspiring discussions. This work is supported by the National Science Foundation, DMR-MPS, Award No. #1709568 (SP) and is benefited by the facilities and staff of the Super Computing System (Spruce Knob) at West Virginia University.

* stefanos.papanikolaou@mail.wvu.edu

[1] R. Asaro and V. Lubarda, *Mechanics of solids and materials* (Cambridge University Press, 2006).
[2] P.M. Anderson, J.P. Hirth, and J. Lothe, *Theory of dislocations* (Cambridge University Press, 2017).
[3] L. Kubin, *Dislocations, mesoscale simulations and plastic flow*, Vol. 5 (Oxford University Press, 2013).
[4] F.R.N. Nabarro, Z.S. Basinski, and D.B. Holt, "The plasticity of pure single crystals," Advances in Physics **13**, 193–323 (1964).
[5] J.A. El-Awady, M. Wen, and N.M. Ghoniem, "The role of the weakest-link mechanism in controlling the plasticity of micropillars," Journal of the Mechanics and Physics of Solids **57**, 32–50 (2009).
[6] S-W. Lee, A.T. Jennings, and J.R. Greer, "Emergence of enhanced strengths and bauschinger effect in conformally passivated copper nanopillars as revealed by dislocation dynamics," Acta Mater. **61**, 1872–1885 (2013).
[7] I. Ryu, W. Cai, W.D. Nix, and H. Gao, "Stochastic behaviors in plastic deformation of face-centered cubic micropillars governed by surface nucleation and truncated source operation," Acta Materialia **95**, 176–183 (2015).
[8] S. Papanikolaou, H. Song, and E. Van der Giessen, "Obstacles and sources in dislocation dynamics: Strengthening and statistics of abrupt plastic events in nanopillar compression," J. Mech. Phys. Solids. **102**, 17 (2015).
[9] S. Papanikolaou, Y. Cui, and N. Ghoniem, "Avalanches and plastic flow in crystal plasticity: an overview," Modelling and Simulation in Materials Science and Engineering **26**, 013001 (2017).
[10] S. Papanikolaou, D.M. Dimiduk, W. Choi, J.P. Sethna, M.D. Uchic, C.F. Woodward, and S. Zapperi, "Quasi-periodic events in crystal plasticity and the self-organized avalanche oscillator," Nature **490**, 517–521 (2012).
[11] S.I. Rao, D.M. Dimiduk, T.A. Parthasarathy, M.D. Uchic, M. Tang, and C.F. Woodward, "Athermal mechanisms of size-dependent crystal flow gleaned from three-dimensional discrete dislocation simulations," Acta Materialia **56**, 3245–3259 (2008).
[12] K. Croes, "Metal Forming: Mechanics and Metallurgy, edited by WF Hosford and R. Caddell," (2011).
[13] B. Devincre, T. Hoc, and L. Kubin, "Dislocation mean free paths and strain hardening of crystals," Science **320**, 1745–1748 (2008).
[14] V.V. Bulatov, L.L. Hsiung, M. Tang, A. Arsenlis, M.C. Bartelt, W. Cai, J.N. Florando, M. Hiratani, M. Rhee, and G. Hommes, "Dislocation multi-junctions and strain hardening," Nature **440**, 1174 (2006).
[15] U.F. Kocks and H. Mecking, "Physics and phenomenology of strain hardening: the FCC case," Progress in materials science **48**, 171–273 (2003).
[16] H. Mecking and U.F. Kocks, "Kinetics of flow and strain-hardening," Acta Metallurgica **29**, 1865–1875 (1981).
[17] N. Goldenfeld, "Lectures on phase transitions and the renormalization group," (1992).
[18] N.M. Ghoniem and R.J. Amodeo, "Computer simulation of dislocation pattern formation." Solid State Phenomena **3 & 4**, 377 (1988).
[19] A. Arsenlis, W. Cai, M. Tang, M. Rhee, T. Oppelstrup, G. Hommes, T.G. Pierce, and V.V. Bulatov, "Enabling strain hardening simulations with dislocation dynamics," Modelling and Simulation in Materials Science and Engineering **15**, 553 (2007).
[20] E. Van der Giessen and A. Needleman, "Discrete dislocation plasticity: a simple planar model," Modelling and Simulation in Materials Science and Engineering **3**, 689 (1995).
[21] D. Weygand, L.H. Friedman, E. Van der Giessen, and

A. Needleman, "Discrete dislocation modeling in three-dimensional confined volumes," Material Science and Engineering **A309-310**, 420 (2001).
[22] G. Po, M.S. Mohamed, T. Crosby, C. Erel, A. El-Azab, and N. Ghoniem, "Recent progress in discrete dislocation dynamics and its applications to micro plasticity," JOM **66**, 2108–2120 (2014).
[23] G. Po and N. Ghoniem, "Mechanics of defect evolution library, model," ⟨https://bitbucket.org/model/model/wiki/home⟩ (2015).
[24] J.A. El-Awady, "Unravelling the physics of size-dependent dislocation-mediated plasticity," Nature Comm. **6** (2015).
[25] A. El-Azab, "Statistical mechanics treatment of the evolution of dislocation distributions in single crystals." Phys. Rev. B **61**, 11956–66 (2000).
[26] Y.S. Chen, W. Choi, S. Papanikolaou, and J.P. Sethna, "Bending crystals: emergence of fractal dislocation structures," Physical review letters **105**, 105501 (2010).
[27] A.H. Cottrell, F.R.N. Nabarro, and M.S. Duesbery, "Commentary. A brief view of work hardening," in *Dislocations in Solids*, Vol. 11 (Elsevier, 2002) pp. vii–xvii.
[28] D.M. Dimiduk, C. Woodward, R. LeSar, and M.D. Uchic, "Scale-free intermittent flow in crystal plasticity," Science **312**, 1188–1190 (2006).
[29] M.D. Uchic, P.A. Shade, and D.M. Dimiduk, "Plasticity of micrometer-scale single crystals in compression," Annual Review of Materials Research **39**, 361–386 (2009).
[30] J.A. El-Awady, S.I. Rao, C. Woodward, D.M. Dimiduk, and M.D. Uchic, "Trapping and escape of dislocations in micro-crystals with external and internal barriers," International Journal of Plasticity **27**, 372–387 (2011).
[31] K. Murasugi, *Knot theory and its applications* (Springer Science & Business Media, 2007).
[32] L.H. Kauffman, *Knots Theory and Physics* (World Scientific: Singapore, 1991).
[33] K. Klenin and J. Langowski, "Computation of writhe in modeling of supercoiled DNA," Biopolymers: Original Research on Biomolecules **54**, 307–317 (2000).
[34] H.K. Moffatt, G.M. Zaslavsky, P. Comte, and M. Tabor, *Topological aspects of the dynamics of fluids and plasmas*, Vol. 218 (Springer Science & Business Media, 2013).
[35] H.K. Moffatt, "The degree of knottedness of tangled vortex lines," Journal of Fluid Mechanics **35**, 117–129 (1969).
[36] T. Hochrainer, "Relative helicity and jog densities in continuum descriptions of dislocations," MRS Advances **1**, 1847–1852 (2016).
[37] W. Püschl, "Models for dislocation cross-slip in close-packed crystal structures: a critical review," Progress in materials science **47**, 415–461 (2002).
[38] G. Saada and J. Washburn, "Interaction between prismatic and glissile dislocations," (1962).
[39] L.K. Wickham, K.W. Schwarz, and J.S. Stölken, "Rules for forest interactions between dislocations," Physical review letters **83**, 4574 (1999).
[40] R. Madec, B. Devincre, and L.P. Kubin, "On the nature of attractive dislocation crossed states," Computational materials science **23**, 219–224 (2002).
[41] V.B. Shenoy, R.V. Kukta, and R. Phillips, "Mesoscopic analysis of structure and strength of dislocation junctions in FCC metals," Physical Review Letters **84**, 1491 (2000).
[42] R. Madec, B. Devincre, and L.P. Kubin, "From dislocation junctions to forest hardening," Physical Review Letters **89**, 255508 (2002).
[43] R. Lagneborg and B-H. Forsen, "A model based on dislocation distributions for work-hardening and the density of mobile and immobile dislocations during plastic flow," Acta Metallurgica **21**, 781–790 (1973).
[44] B Devincre and L.P. Kubin, "Simulations of forest interactions and strain hardening in fcc crystals," Modelling Simul. Mater. Sci. Eng. **2**, 559 (1994).
[45] U.F. Kocks, "A statistical theory of flow stress and work-hardening," Phil Mag **13**, 541 (1966).
[46] T. Takeuchi, "Work hardening of copper single crystals with multiple glide orientations," Transactions of the Japan Institute of Metals **16**, 629–640 (1975).
[47] P. Cermelli and M.E. Gurtin, "On the characterization of geometrically necessary dislocations in finite plasticity," Journal of the Mechanics and Physics of Solids **49**, 1539–1568 (2001).
[48] E. Kröner, "Allgemeine kontinuumstheorie der versetzungen und eigenspannungen," Archive for Rational Mechanics and Analysis **4**, 273 (1959).
[49] E.H. Lee, "Elastic-plastic deformation at finite strains," (1969).
[50] B. Devincre, L. Kubin, and T. Hoc, "Physical analyses of crystal plasticity by DD simulations," Scripta Materialia **54**, 741–746 (2006).
[51] G.Z. Voyiadjis and M. Yaghoobi, "Size and strain rate effects in metallic samples of confined volumes: Dislocation length distribution," Scripta Materialia **130**, 182–186 (2017).
[52] C.R. Weinberger and W. Cai, "The stability of Lomer–Cottrell jogs in nanopillars," Scripta Materialia **64**, 529–532 (2011).
[53] N. Hansen and D.A. Hughes, "Analysis of large dislocation populations in deformed metals," physica status solidi (a) **149**, 155–172 (1995).
[54] C. Hong, X. Huang, and G. Winther, "Dislocation content of geometrically necessary boundaries aligned with slip planes in rolled aluminium," Philosophical Magazine **93**, 3118–3141 (2013).

Supplementary Information: The Λ-invariant and topological pathways to influence the strength of sub-micron crystals

Stefanos Papanikolaou[†1,2] and Giacomo Po[3]

[1] *Department of Mechanical & Aerospace Engineering, West Virginia University, 395 Evansdale Drive, Morgantown, WV, 26506-6070.*
[2] *Department of Physics & Astronomy, West Virginia University, 135 Willey St, Morgantown, WV 26506-6070.*
[3] *Department of Mechanical & Aerospace Engineering, University of Miami, 1251 Memorial Drive, Coral Gables, FL 33146*

(Dated: April 4, 2020)

In this Supplementary Information, we provide further details on the calculations discussed in the main text.

I. Λ AND LINKING NUMBERS L_{ij}

We initially discuss the proof of Eq.3 in the main text, which forms a major cornerstone of this work. Namely, Eq.3 of the main text states that the topological invariant Λ which involves doubles integrals over all loop segments, is directly connected to a simple sum of dot products, something that can reduce numerical calculation burden and also confirms the topological character of Λ. For clarity, Eq.3 of the main text states that:

$$\Lambda = -\frac{1}{b^2}\sum_{i,j} L_{ij}\mathbf{b}_i\cdot\mathbf{b}_j \tag{S-I.1}$$

where L_{ij} is the linking number between loops i and j, while $\mathbf{b}_i$ and $\mathbf{b}_j$ are their respective Burgers vectors. In order to prove Eq. S-I.1, we will use some identities of dislocation theory (please see Ref. 2 in the main text for details),

$$\oint_{\partial\mathcal{S}} \epsilon_{klm} T dL_k = \int_{\mathcal{S}} (T_{,m} dS_l - T_{,l} dS_m) \tag{S-I.2}$$

$$\oint_{\partial\mathcal{S}} T dL_i = \int_{\mathcal{S}} \epsilon_{ijk} T_{,k} dS_j \tag{S-I.3}$$

$$\begin{aligned}
&\frac{1}{4\pi}\oint\oint \frac{\boldsymbol{r}_1-\boldsymbol{r}_2}{\|\boldsymbol{r}_1-\boldsymbol{r}_2\|^3}\cdot(d\boldsymbol{r}_1\times d\boldsymbol{r}_2) = \\
&\quad = \frac{1}{4\pi}\oint\oint \left(\frac{1}{R}\right)_{,j} \epsilon_{jkl} dx_k^{(A)} dx_l^{(B)} \\
&\quad = \frac{1}{4\pi}\oint\oint \frac{1}{2} R_{,ppj}\,\epsilon_{jkl} dx_k^{(A)} dx_l^{(B)}
\end{aligned} \tag{S-I.4}$$

Then, by starting with the definition of Λ:

$$\Lambda = \frac{1}{b^2}\int d^3x \beta^E\cdot(\nabla\times\beta^E) = \frac{1}{b^2}\int d^3x \beta^E_{ij}\alpha_{ij} \tag{S-I.5}$$

It is straightforward to expand,

$$\begin{aligned}
b^2\Lambda &= \int_{\mathbb{R}^3} \beta^E_{ij}\alpha_{ij}\,\mathrm{d}V \\
&= \int_{\mathbb{R}^3} \beta^E_{ij}\sum_A \oint_{\mathcal{L}^A} \delta(\boldsymbol{x}-\boldsymbol{x}')b_i^A\,\mathrm{d}\ell'_j\,\mathrm{d}V \\
&= \sum_A b_i^A \oint_{\mathcal{L}^A} \beta^E_{ij}\,\mathrm{d}\ell_j \\
&= \sum_A b_i^A \oint_{\mathcal{L}^A} u_{i,j}\,\mathrm{d}\ell_j \mp \sum_A b_i^A \oint_{\mathcal{L}^A} \beta^P_{ij}\,\mathrm{d}\ell_j \\
&= \sum_A b_i^A \oint_{\mathcal{L}^A}\sum_B \int_{\mathcal{S}^B} b_i^B \delta(\boldsymbol{x}-\boldsymbol{x}')\,\mathrm{d}S'_j\,\mathrm{d}\ell_j \\
&= -\frac{1}{4\pi}\sum_A\sum_B b_i^A b_i^B \oint_{\mathcal{L}^A}\int_{\mathcal{S}^B}\left(\frac{1}{R}\right)_{,pp}\mathrm{d}S'_j\,\mathrm{d}\ell_j \\
&= -\frac{1}{4\pi}\sum_A\sum_B b_i^A b_i^B \oint_{\mathcal{L}^A}\int_{\mathcal{S}^B}\left(\frac{1}{R}\right)_{,pj}\mathrm{d}S'_p\,\mathrm{d}\ell_j \\
&\quad -\frac{1}{4\pi}\sum_A\sum_B b_i^A b_i^B \oint_{\mathcal{L}^A}\oint_{\mathcal{L}^B}\epsilon_{kjp}\left(\frac{1}{R}\right)_{,p}\mathrm{d}\ell'_k\,\mathrm{d}\ell_j \\
&= -\frac{1}{4\pi}\sum_A\sum_B b_i^A b_i^B \oint_{\mathcal{L}^A}\oint_{\mathcal{L}^B}\epsilon_{kjp}\left(\frac{1}{R}\right)_{,p}\mathrm{d}\ell'_k\,\mathrm{d}\ell'_j \\
&= -\sum_{A,B} L_{AB}\mathbf{b}_A\cdot\mathbf{b}_B
\end{aligned} \tag{S-I.6}$$

II. THE Λ DYNAMICS

For x-y torsion $\beta_E \sim \hat{\theta}$ (primarily) in cylindrical coordinates, since most dislocations (screw) are lying along z-axis. Moreover, dynamics during compression in a torsioned specimen implies that $J \sim -\hat{r}$ in cylindrical coor-

[†]stefanos.papanikolaou@mail.wvu.edu

dinates. (to check it again)

In order to be careful, one needs to carefully perform these calculations using the proper tensorial indices. In this context, it is important to clarify that:

1. For α_{ij}: i indexes the dislocation line vector $\mathbf{t}$ that the dislocation is tangent to, while j indexes the Burgers vector $\mathbf{b}$.

2. For J_{ij} and a single dislocation line moving with velocity $\mathbf{v}$, $J_{ij} = \epsilon_{ikm} t_k b_j v_m \delta(\mathbf{x})$ at some location $\mathbf{x}$. So, i labels the cross product $\mathbf{t} \times \mathbf{v}$.

3. Also, for J_{ij} (if overdamped dynamics is considered): it is written as $J_{ij} = M \epsilon_{ikm} F_m \alpha_{kj}$, where M is an approriately defined dislocation mobility factor and F_m is the PK force on the dislocation density α_{kj} ($F \times \alpha$ making sure that a dislocation density moves perpendicularly to the dislocation line vector).

4. For β^E_{ij}: i labels the strain direction, while j the component of the displacement vector.

5. We need to assume a particular dynamics law for the elastic and plastic distortion in order to proceed. Assuming the Nye dislocation tensor,

$$\alpha_{ij} = -\epsilon_{ilm} \partial_l \beta^P_{mj} = \epsilon_{ilm} \partial_l \beta^E_{mj} \tag{S-II.1}$$

we can assume a generic conservation law for the Burgers' vector:

$$\partial_t \alpha_{ij} = -\epsilon_{ilm} \partial_l J_{mj} \tag{S-II.2}$$

which also implies,

$$\partial_t \beta^E_{ij} = -J_{ij} \tag{S-II.3}$$

The ultimate target is to understand and predict which loading modes can lead to a large increase of the dislocation helicity, and consequently the elastic energy of the crystal. Assuming that the volume V is fixed, with ∂V a boundary surface, then, if the helicity is defined as:

$$\Lambda = \frac{1}{b^2} \int_V dV \beta^E_{kl} \epsilon_{kmn} \partial_m \beta^E_{nl} \tag{S-II.4}$$

or

$$\Lambda = \frac{1}{b^2} \int_V dV \beta^E_{kl} \alpha_{kl} \tag{S-II.5}$$

then the temporal variation of dislocation helicity is derived by direct differentiation:

$$b^2 \frac{\partial \Lambda}{\partial t} = \int_V dV \frac{\partial \beta^E_{kl}}{\partial t} \alpha_{kl} + \int_V dV \beta^E_{kl} \frac{\partial \alpha_{kl}}{\partial t} \tag{S-II.6}$$

Now we can use Eqs. S-II.2 and S-II.3, showing that

$$b^2 \frac{\partial \Lambda}{\partial t} = -\int_V dV J_{kl} \alpha_{kl} - \int_V dV \beta^E_{kl} \epsilon_{kjm} \partial_j J_{ml} \tag{S-II.7}$$

Now, we may use integration by parts in the second integral:

$$b^2 \frac{\partial \Lambda}{\partial t} = -\int_V dV J_{kl} \alpha_{kl} - \int_{\partial V} dS_j \beta^E_{kl} \epsilon_{kjm} J_{ml} + \int_V dV \partial_j \beta^E_{kl} \epsilon_{kjm} J_{ml} \tag{S-II.8}$$

which is equal to:

$$b^2 \frac{\partial \Lambda}{\partial t} = -\int_V dV J_{kl} \alpha_{kl} - \int_V dV \alpha_{ml} J_{ml} - \int_{\partial V} dS_j \beta^E_{kl} \epsilon_{kjm} J_{ml} \tag{S-II.9}$$

or

$$b^2 \frac{\partial \Lambda}{\partial t} = -2 \int_V dV J_{kl} \alpha_{kl} + \int_{\partial V} dS_j \epsilon_{jkm} \beta^E_{kl} J_{ml} \tag{S-II.10}$$

The first integral (volume) is identically zero for the conservative dynamics, since $J_{kl}\alpha_{kl} = \epsilon_{kij}\alpha_{il}F_j\alpha_{kl} \equiv \epsilon_{kij}\alpha_{il}\alpha_{kl}F_j$ (zero by reversing k, i). Thus, it is proven that dislocation helicity is conserved by volume dynamics.

The second integral is equivalent to:

$$\int_{\partial V} d\mathbf{S} \cdot (\beta^E \times J) \tag{S-II.11}$$

III. Λ AT LARGE DEFORMATIONS

In the deformed configuration $\mathbf{x}$ (also labeled by above symbols), one can still define simply the burgers vector as a smooth loop/surface integral:

$$\mathbf{b} = \int_{\partial S} \mathbf{F^{e-1}} d\mathbf{x} = \int_S (\nabla \times \mathbf{F^{e-1}})^\tau \tilde{\mathbf{n}} d\tilde{A} \tag{S-III.1}$$

where $\mathbf{F^{e-1}} = (\mathbf{F^e})^{-1}$, $\mathbf{F} = \mathbf{F^e F^p}$ the Kröner-Lee decomposition, $\mathbf{F} = \nabla y$ the deformation gradient, and $\mathbf{n}$ is the vector normal to the area S. Also, it is important to remember that,

$$(\nabla \times \mathbf{T})_{ij} = \epsilon_{irs} \frac{\partial T_{js}}{\partial x_r} \tag{S-III.2}$$

with respect to the orthonormal basis vectors.

At large deformations, it is important to remember that the deformed coordinates are connected to the *reference* configuration through the relation:

$$\tilde{\mathbf{n}}d\tilde{A} = J^e\mathbf{F}^{\mathbf{e}-\tau}\mathbf{n}dA \tag{S-III.3}$$

Regarding the $\Lambda-$invariant, it is transparent how to extend our definitions in the large deformation regime, in the deformed coordinates. Namely, one can define,

$$\Lambda = \frac{1}{b^2}\int \mathbf{F^{e-1}}\cdot(\nabla\times\mathbf{F^{e-1}})^{-\tau}d\tilde{V} \tag{S-III.4}$$

and in the **reference** frame:

$$\Lambda = \frac{1}{b^2}\int J^e\mathbf{F^{e-1}}\cdot(\nabla\times\mathbf{F^{e-1}})^{-\tau}\cdot\mathbf{F}^{\mathbf{e}-\tau}d\tilde{V} \tag{S-III.5}$$

Eq. S-III.5 represents the large deformation definition of the $\Lambda-$invariant.

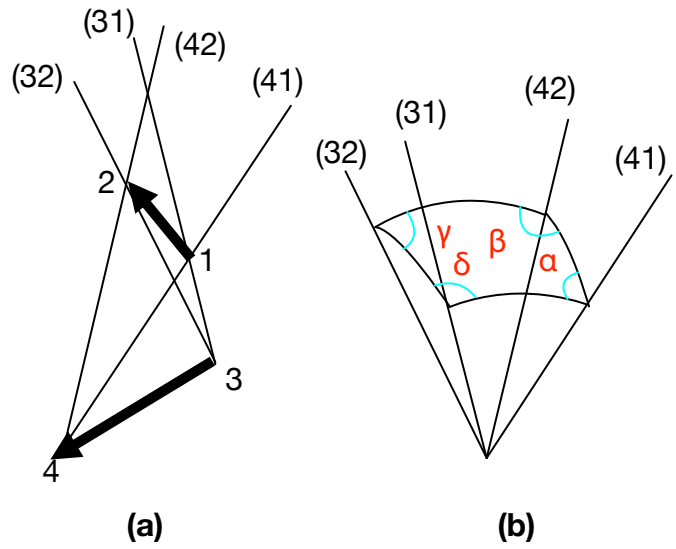

FIG. 1: **Calculation of the Gauss integral along two straight segments arbitrary oriented in space (a)** The arbitrary vector $\mathbf{r}_{12}$ has the beginning and the end at the points 1 and 2, and the vector $\mathbf{r}_{34}$ has the beginning and the end at the points 3 and 4, respectively. **(b)** The quadrangle on a unit sphere is constructed for the given pair of segments, $\mathbf{r}_{12}$ and $\mathbf{r}_{34}$.

IV. THE CALCULATION OF Λ IN DISCRETE DISLOCATION DYNAMICS

In order to calculate Λ for a dislocation ensemble, a procedure is followed that tracks the calculations of helicity in other fields of physics (see for example Ref.[28] of the main text).

It is critical that the dislocation ensemble is originally composed of non-touching prismatic loops in the finite pillar volume. In the simulations described in the manuscript, these loops are created by first picking randomly any node of the finite element mesh, and then the loop dimensions are picked by using a flat random distribution from the negative (positive) mesh side length as minimum (maximum). As DDD proceeds, loops may end on an open surface; such loops are assumed to close (through the open surface) in a specific way that remains the same throughout the simulation. For each pair of non-touching loops i and j, the procedure described in Ref.[27] can be used to calculate the pair's linking number. The linking number is calculated through the double integral:

$$L_{ij} = \frac{1}{4\pi}\int_{C_i}\int_{C_j}\frac{(d\mathbf{r}_j\times d\mathbf{r}_i)\mathbf{r}_{ij}}{r_{ij}^3} \tag{S-IV.1}$$

where $\mathbf{r}_1$ and $\mathbf{r}_2$ are the points passing along the curves C_i and C_j, $\mathbf{r}_{12}=\mathbf{r}_2-\mathbf{r}_1$, $r_{12}=|\mathbf{r}_{12}|$. More succinctly,

$$L_{ij} = \frac{1}{4\pi}\int_{C_i}\int_{C_j}d\Omega(\mathbf{r}_i,\mathbf{r}_j) \tag{S-IV.2}$$

where $\Omega(\mathbf{r}_i,\mathbf{r}_j)=\frac{(d\mathbf{r}_j\times d\mathbf{r}_i)\mathbf{r}_{ij}}{r_{ij}^3}$.

If the loops i,j are discretized onto polygons of N_i, N_j segments, then

$$L_{ij} = \frac{1}{4\pi}\sum_{k=1}^{N_i}\sum_{l=1}^{N_j}\Omega_{kl} \tag{S-IV.3}$$

where $\Omega_{kl}/4\pi$ is the Gauss integral along the segments k,l ($\Omega_{kl}=\Omega_{lk}$, Ω_{kk}=0, $\Omega_{k,k+1}=0$). Also, for a pair of segments k,l arbitrary oriented in space, one may apply a pure geometrical approach:

If points 1 and 2 are the beginning and end of the first segment $\mathbf{r}_{12}$ and points 3 and 4 are the beginning and end of the second segment $\mathbf{r}_{34}$, then the absolute value of the Gauss integral multiplied by 4π is the solid angle Ω^*:

$$\Omega^* = \alpha+\beta+\gamma+\delta-2\pi \tag{S-IV.4}$$

where α, β, γ and δ are the angles of the quadrangle shown in Fig. 1. The angles can be found by considering

$$\mathbf{n}_1 = \frac{\mathbf{r}_{13}\times\mathbf{r}_{14}}{|\mathbf{r}_{13}\times\mathbf{r}_{14}|} \tag{S-IV.5}$$

$$\mathbf{n}_2 = \frac{\mathbf{r}_{14}\times\mathbf{r}_{24}}{|\mathbf{r}_{14}\times\mathbf{r}_{24}|} \tag{S-IV.6}$$

$$\mathbf{n}_3 = \frac{\mathbf{r}_{24}\times\mathbf{r}_{23}}{|\mathbf{r}_{24}\times\mathbf{r}_{23}|} \tag{S-IV.7}$$

$$\mathbf{n}_4 = \frac{\mathbf{r}_{23}\times\mathbf{r}_{13}}{|\mathbf{r}_{23}\times\mathbf{r}_{13}|} \tag{S-IV.8}$$

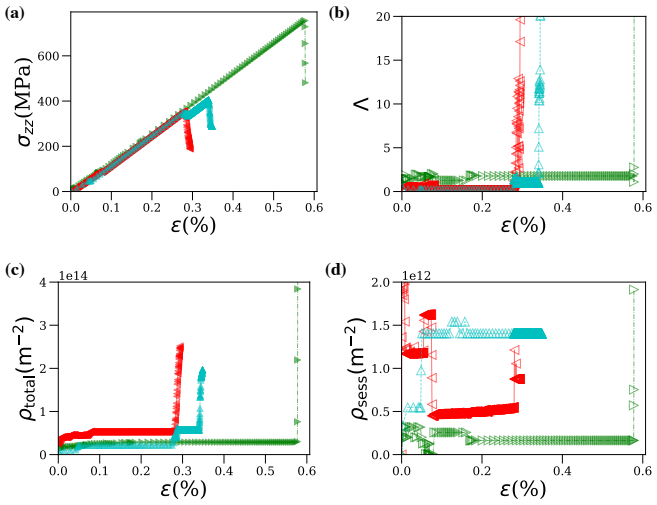

FIG. 2: **Depositing & Testing Entanglement For Various Discrete Dislocation Densities: Uniaxial compression of sub-micron volumes.** This is a broken-down version of Fig.4(c-d) in the main text. Every point corresponds to a uniaxial compression simulation of distinct initial conditions at a target ρ_0: (ρ_0 : {■ : 10^{13}/m^2}, {▶: 2×10^{13}/m^2}, {◀: 4×10^{13}/m^2}, {▲ : 8×10^{13}/m^2}, {▼ : 10^{14}/m^2}). In **(a)** and **(b)**, an excerpt of the response of three sample initial conditions are shown in detail to demonstrate the major effect that heavily entangled have on mechanical response. The loading stress σ_{zz} as function of the applied axial zz strain ϵ is shown in **(a)** with solid symbols. The Λ configurational value as function of the applied axial zz strain ϵ is shown in **(b)** with open symbols. Analogously, in **(c) and (d)**, the total and sessile dislocation density are respectively shown. The sessile dislocation density increases roughly linearly with Λ_0 while yield stress quickly saturates. ρ_0 values are given for the conditions used in **(a-d)**: ({▲ : 8×10^{12}/m^2}, {▶: 10^{13}/m^2}, {◀: 2×10^{13}/m^2}).

and then,

$$\alpha = \pi/2 + \arcsin(\mathbf{n}_1\mathbf{n}_2) \quad \text{(S-IV.9)}$$
$$\beta = \pi/2 + \arcsin(\mathbf{n}_2\mathbf{n}_3) \quad \text{(S-IV.10)}$$
$$\gamma = \pi/2 + \arcsin(\mathbf{n}_3\mathbf{n}_4) \quad \text{(S-IV.11)}$$
$$\delta = \pi/2 + \arcsin(\mathbf{n}_4\mathbf{n}_1) \quad \text{(S-IV.12)}$$

with

$$\Omega^* = \arcsin(\mathbf{n}_1\mathbf{n}_2) + \arcsin(\mathbf{n}_2\mathbf{n}_3) + \arcsin(\mathbf{n}_3\mathbf{n}_4) + \arcsin(\mathbf{n}_4\mathbf{n}_1) \quad \text{(S-IV.13)}$$

Finally,

$$\frac{\Omega}{4\pi} = \frac{\Omega^*}{4\pi}\text{sign}((\mathbf{r}_{34}\times\mathbf{r}_{12})\mathbf{r}_{13}) \quad \text{(S-IV.14)}$$

As the simulation continues, dislocation touching may happen that can lead to junction formation. In our calculation of Λ, we track its evolution and we follow the rule that once a touching/junction takes place between two loops, then the mutual linking number remains the same as before the touching event, until they stop touching. It is worth pointing out that tracking of dislocation loops does not stop at any stage of the simulation, even if junctions are present (composed of segments of prior defined dislocation loops).

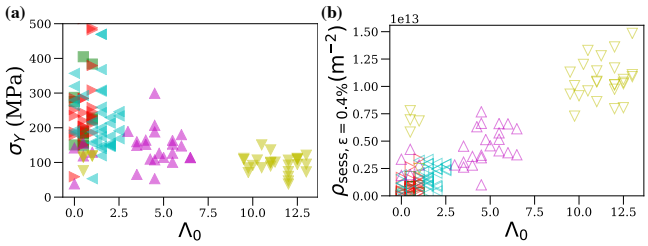

FIG. 3: **Yield stress, ρ_{sess} and Λ during uniaxial compression of sub-micron volumes.** Initial sessile junction density is always zero. This is a broken-down version of Fig.4(b) in the main text. By repeating the process shown in Fig. 2, we collect **(a)** the yield stress value σ_Y(MPa units) and **(b)** the sessile dislocation density, as averages in the range 0.1% and 0.2% strain, and they are shown against the initial Λ_0. Each point represents a completed simulation of uniaxial compression of a 0.5μm-diameter pillar and aspect ratio 4. Every marker's color/type signify a target ρ_0: (ρ_0 : {■ : 10^{13}/m^2}, {▶: 2×10^{13}/m^2}, {◀: 4×10^{13}/m^2}, {▲ : 8×10^{13}/m^2}, {▼ : 10^{14}/m^2}).

V. MORE DETAILS ON NUMERICAL CALCULATIONS AND FIGURES OF MAIN TEXT

In the following, we discuss further details of the figures in the main text, breaking them down and providing a number of numerical factors needed for their reproducibility. First, in Fig. 2, we show 3 cases of uniaxial compression and their effect on Λ. Λ can grow quickly during an avalanche, and this is seen through three samples at different initial dislocation densities of dipolar prismatic loops with symbols: ({▲ : 8×10^{12}/m^2}, {▶: 10^{13}/m^2}, {◀: 2×10^{13}/m^2}. In addition, as it is seen in Fig. 2(a-d), as the loading stress decreases during an avalanche and Λ increases, there is an associate increase of the total and sessile dislocation densities. Nevertheless, the behavior of the sessile dislocation density appears highly correlated with the Λ response, even though it is virtually impossible to identify analogous signatures on either the loading stress or the total dislocation density.

In Fig. 3, we show statistics of the uniaxial compression yield stress and the sessile dislocation density at a

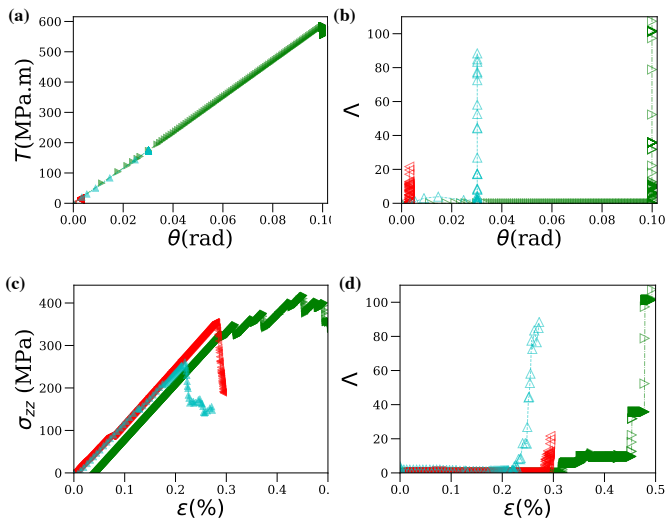

FIG. 4: **Engineering Entanglement By Controlling Prior Torsion Strains**. This is a broken-down version of Fig.5(c,d) in the main text. A 2-step protocol is followed where a dislocation loop configuration at density ρ_0 is prepared, and then: **(a)** a torsional load is applied on top/bottom pillar surfaces up to pre-chosen torsion angle θ_0, and (c) uniaxial compression is applied towards yield. Three samples, distinguished by θ_0 (0.003, 0.03, 0.1)rad, and particular initial conditions with, $\{\rho_0, \theta_0\} \rightarrow \Big($▶: $[10^{13}/\mathrm{m}^2, 0.1]$, ◀: $[2\times10^{13}/\mathrm{m}^2, 3\times10^{-3}]$, ▲ : $[2\times10^{13}/\mathrm{m}^2, 3\times10^{-2}]\Big)$, are shown for **(a)** Torsion T (filled symbols) and **(b)** Λ (open symbols) *vs.* torsion angle θ in the first step of the process, and **(c)** subsequent loading stress σ_{zz} (filled symbols) and **(d)** Λ (open symbols) *vs.* axial strain ϵ in the second step.

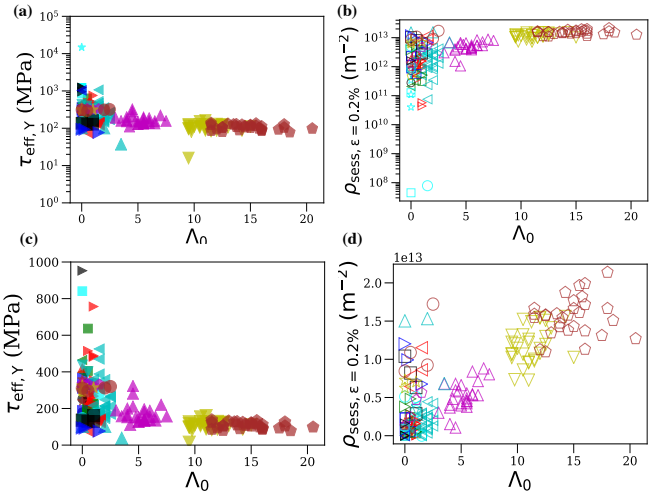

FIG. 5: **Engineering Entanglement By Controlling Prior Torsion Strains – Statistics**. This is a broken-down version of Fig.5(b) in the main text. **(a)** or **(c)**: Yield stress (filled symbols) *vs.* Λ_0 and **(a)** or **(c)**: sessile dislocation density (open symbols) at the yield point for a variety of initial conditions and torsions $\rho_0 \in (5\times10^{12}, 2\times10^{14})$ and $T \in \{10^{-5}, 0.1\}$. **(a)** and **(b)** are in the log scale, demonstrating outlier points at small Λ_0, while **(c)** and **(d)** are in linear scale (as in the main text).

prescribed strain value 0.4% with respect to the value of Λ_0. Sample size is fixed at diameter $4000b \simeq 0.5\mu$m and aspect ratio 4. The yield stress is estimated through an average of the stress values at a prescribed range of strains $(0.1\%, 0.2\%)$. Given that dipolar prismatic loops are initially distributed at random sizes, Λ_0 displays a dependence on the initial dislocation density ρ_0. As the initial dislocation density changes, Λ_0 is modified as well. As it is seen in Fig. 3(a), yield stress data for $\Lambda_0 \lesssim 2.0$ display strong size dependence and stochasticity. In addition, the sessile dislocation density at strain 0.4% displays a linear increase with Λ_0. Also, it is worth noting that $\Lambda_0 \lesssim 2.0$ coincides with $\rho_0 < 5\times10^{13}$, given the way of preparing the initial dislocation configuration. It is seen that configurations with $\Lambda_0 > 2$ display bulk-like yield stress and high sessile dislocation density.

in Fig. 4, we show 3 cases of our 2-stage protocol that may engineer high Λ, while starting from low dislocation densities. Sample size is fixed at diameter $4000b \simeq 0.5\mu$m and aspect ratio 4. The 2-stage protocol is demonstrated in the figure. A torsional load is applied on the top and bottom surfaces of the samples until a prescribed torsional angle θ_0. In Fig. 4, the torsional angle for the three cases is 0.003 rad, 0.03 rad and 0.1 rad for left-pointing triangles, top-pointing triangles and right-pointing triangles respectively. As shown in Fig. 4(a), the torsional load increases linearly with the torsional angle until the target torsional angle. As shown in Fig. 4(b), Λ grows quickly at the torsional angle. While torsional angle remains fixed, the second stage of the protocol involves uniaxial compression along the pillar axis, and the loading stress σ_{zz} is shown in Fig. 4(c). During uniaxial loading, Λ grows quickly as the loading strain increases beyond 0.2%.

In Fig. 5, we show statistics of the effective yield stress (including the torsional load) and the sessile dislocation density at a prescribed strain value 0.4% with respect to the value of Λ_0 at the start of the uniaxial compression, just after torsion is completed. Sample size is fixed at diameter $4000b \simeq 0.5\mu$m and aspect ratio 4. The yield stress is estimated through an average of the stress values at a prescribed range of strains $(0.1\%, 0.2\%)$. Both in **(a), (b)** linear and **(c), (d)** log scales, the effective yield stress displays a fast saturation with Λ_0, while the sessile dislocation density linearly increases. The similarity of the behavior with the one shown in Fig. 3 is striking, pointing again to a critical $\Lambda_c \simeq 2$, even though the generation of topological entanglement is drastically different. Configurations with $\Lambda_0 > 2$ display bulk-like yield stress and high sessile dislocation density.

In Fig. 6, we show sample initial dislocation configura-

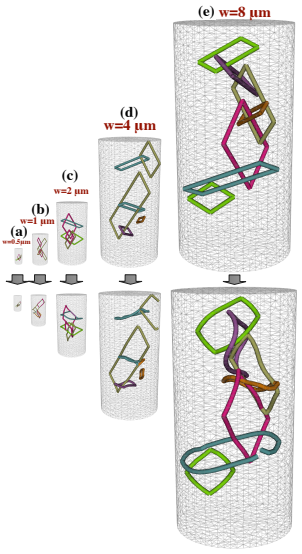

FIG. 6: **Relatively sized images of initial dislocation configurations at various widths with small** Λ. The cases are for **(a):** $w = 0.5\mu$m, $\rho_0 = 2 \times 10^{13}/m^2$, **(b):** $w = 1\mu$m, $\rho_0 = 5 \times 10^{12}/m^2$, **(c):** $w = 2\mu$m, $\rho_0 = 1.2 \times 10^{12}/m^2$ **(d):** $w = 4\mu$m, $\rho_0 = 3.1 \times 10^{11}/m^2$ **(e):** $w = 8\mu$m, $\rho_0 = 10^{11}/m^2$

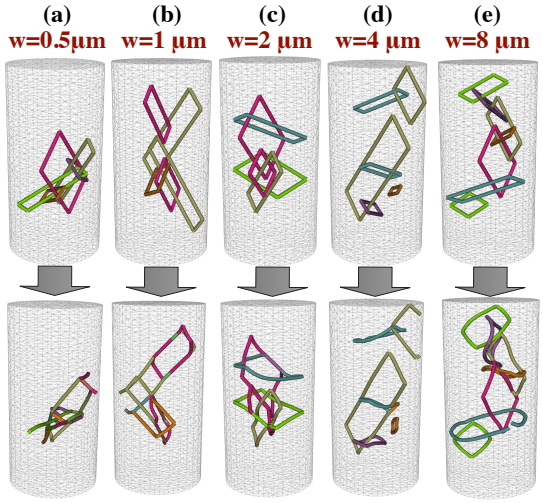

FIG. 7: **Equally-sized images of initial dislocation configurations at various widths with small** Λ. The cases are for **(a):** $w = 0.5\mu$m, $\rho_0 = 2 \times 10^{13}/m^2$, **(b):** $w = 1\mu$m, $\rho_0 = 5 \times 10^{12}/m^2$, **(c):** $w = 2\mu$m, $\rho_0 = 1.2 \times 10^{12}/m^2$ **(d):** $w = 4\mu$m, $\rho_0 = 3.1 \times 10^{11}/m^2$ **(e):** $w = 8\mu$m, $\rho_0 = 10^{11}/m^2$

tions that have $\Lambda_0 < 2$ collectively, at all the system sizes studied in this work, also keeping a relative size difference to demonstrate the simulation's difference. The pillar diameters from left to right increase from $w = 0.5\mu$m to $w = 1.0\mu$m, $w = 2.0\mu$m, $w = 4.0\mu$m, $w = 8.0\mu$m. The upper row shows the initial dislocation configuration, while the lower row shows the configurational evolution

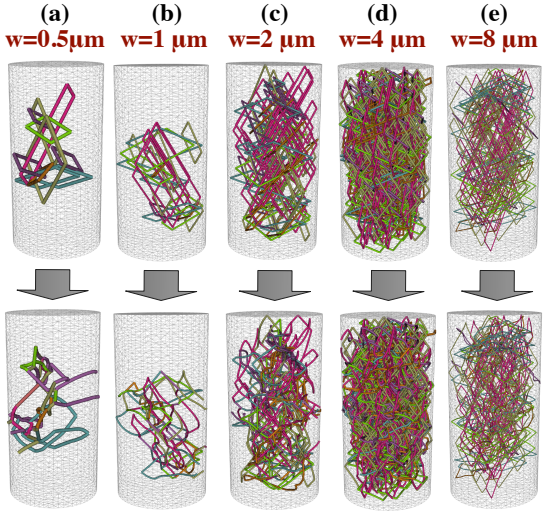

FIG. 8: **Equally-sized images of initial dislocation configurations at various widths with large** Λ. The cases are for **(a):** $w = 0.5\mu$m, $\rho_0 = 4 \times 10^{13}/m^2$, **(b):** $w = 1\mu$m, $\rho_0 = 2 \times 10^{13}/m^2$, **(c):** $w = 2\mu$m, $\rho_0 = 2 \times 10^{13}/m^2$ **(d):** $w = 4\mu$m, $\rho_0 = 2 \times 10^{13}/m^2$ **(e):** $w = 8\mu$m, $\rho_0 = 2 \times 10^{13}/m^2$

after 1000 loading steps at 10^3/s.

In Fig. 7, we show sample initial dislocation configurations that have $\Lambda_0 < 2$ collectively, at all the system sizes studied in this work, while keeping the sample size intact and making the dislocation lines visible in each case by thickening them. It is important to notice that dislocation lines have a core size that should become relatively less visible in larger samples. The pillar diameters and configurations are the same as Fig. 6.

In Fig. 6, we show sample initial dislocation configurations that have $\Lambda_0 > 3$ collectively, at all the system sizes studied in this work, also keeping the sample sizes identical for better configurational visibility. The pillar diameters from left to right increase from $w = 0.5\mu$m to $w = 1.0\mu$m, $w = 2.0\mu$m, $w = 4.0\mu$m, $w = 8.0\mu$m. The upper row shows the initial dislocation configuration, while the lower row shows the configurational evolution after 1000 loading steps at $10^{-10}/b$(!!!). The initial Λ_0 from left to right in these configurations is: $\Lambda_0(w = 0.5\mu m) = 6.0$, $\Lambda_0(w = 1.0\mu m) = 13.5$, $\Lambda_0(w = 2.0\mu m) = 77.5$, $\Lambda_0(w = 4.0\mu m) = 603.75$, $\Lambda_0(w = 8\mu m) = 128.0$.